Title

Remodeling of Architected Mesenchymal Microtissues Generated on Mechanical Metamaterials

Journal

3D Printing and Additive Manufacturing, 9(6)

ISSN

2329-7662

Authors

Wang, Chenyan

Vangelatos, Zacharias

Winston, Tackla

et al.

Publication Date

2022-12-01

DOI

10.1089/3dp.2021.0091

Peer reviewed

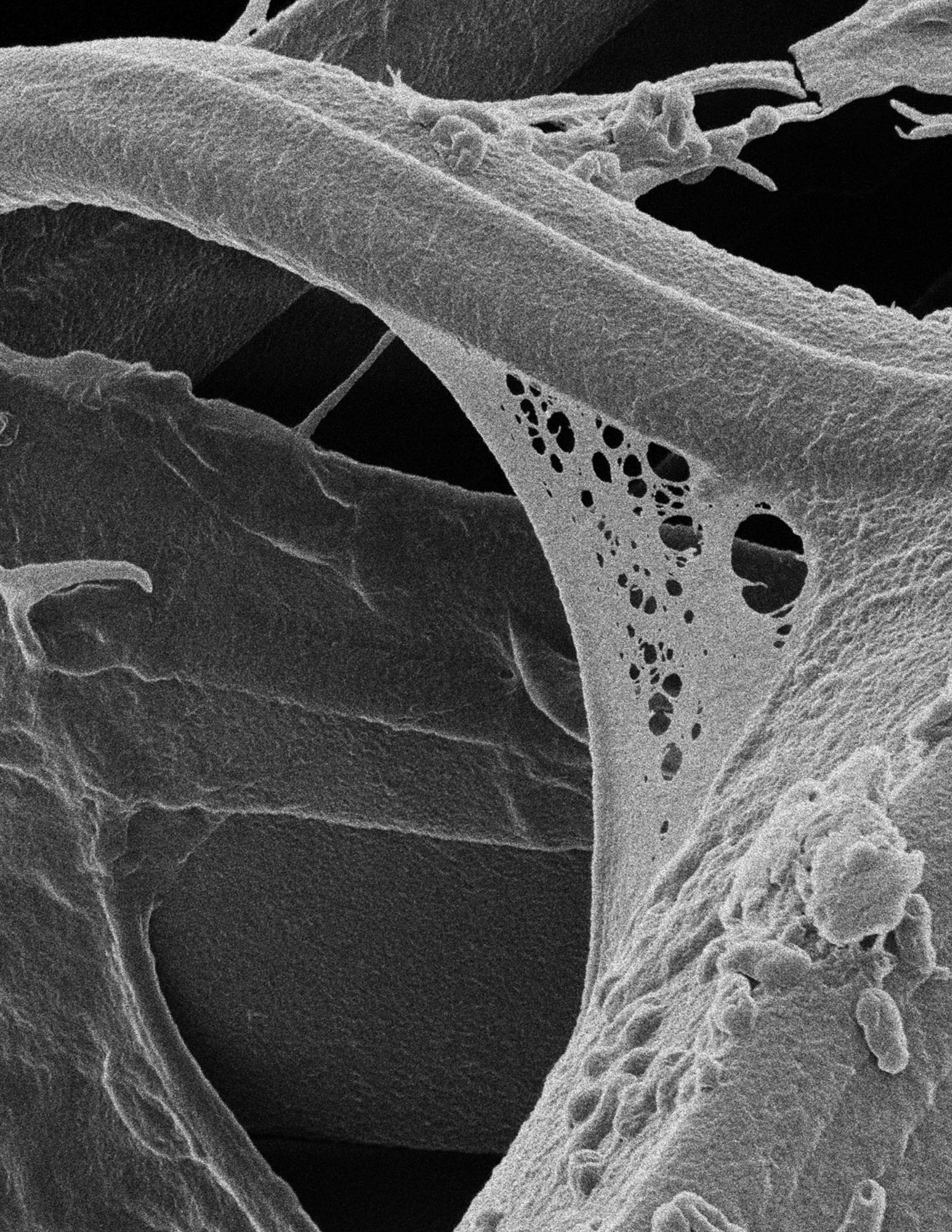

3D PRINTING AND ADDITIVE MANUFACTURING
Volume 9, Number 6, 2022

DOI: 10.1089/3dp.2021.0091

ORIGINAL ARTICLE

Remodeling of Architected Mesenchymal Microtissues Generated on Mechanical Metamaterials

Chenyan Wang,[1,2,*] Zacharias Vangelatos,[3,*] Tackla Winston,[1,2] Shiyang Sun,[1,2] Costas P. Grigoropoulos,[3] and Zhen Ma[1,2]

Abstract

Mechanical metamaterials constitute a nascent category of architected structures comprising arranged periodic components with tailored geometrical features. These materials are now being employed as advanced medical implants due to their extraordinary mechanical properties over traditional devices. Nevertheless, to achieve desired tissue integration and regeneration, it is critical to study how the microarchitecture affects interactions between metamaterial scaffolds and living biological tissues. Based on human induced pluripotent stem cell technology and multiphoton lithography, we report the establishment of an *in vitro* microtissue model to study the integration and remodeling of human mesenchymal tissues on metamaterial scaffolds with different unit geometries. Microtissues showed distinct tissue morphologies and cellular behaviors between architected octet-truss and bowtie structures. Under the active force generated from mesenchymal tissues, the octet-truss and bowtie metamaterial scaffolds demonstrated unique instability phenomena, significantly different from uniform loading using conventional mechanical testing.

Keywords: multiphoton lithography, mechanical metamaterials, *in vitro* tissue model, human induced pluripotent stem cells, mechanical instability

Introduction

MECHANICAL METAMATERIALS ARE architected structures possessing microscale or nanoscale topological features that are assembled in a specialized order. The material properties of metamaterials depend on the geometry of the unit structure. The rational design of the unit structure and arrangement enables superior material properties at macroscales over natural materials.[1,2] For instance, pentamode metamaterials, which are made of face-centered cubic unit cell structures, have high bulk modulus, but very low shear modulus.[3] This enables them to function as liquid structures and inherit controllable wave propagation. Moreover, novel metamaterial designs encompassing hyperelastic behavior have been proposed to employ brittle materials for fabricating devices that require large, but recoverable, deformations.

For applications in biomedical engineering, mechanical metamaterials have been mostly used in design and fabrication of metaimplants.[4,5] By combining metamaterials with different degrees of auxeticity in a hip implant design, implant–bone integration and implant longevity were substantially improved.[6] To improve host tissue integration by manipulating the anisotropy of the implant (i.e., the Zener ratio),[7] a combination of auxetic and isotropic structures makes it possible to fabricate the metaimplant possessing the failure resistance and adjustable anisotropy that could match that of specific tissues.

Despite these incipient results of metaimplants, the use of metamaterials is still focused on optimization of implant adaptivity to native conditions. Tissue–scaffold interaction between mechanical metamaterials and biological tissues is still underexplored, while unraveling this response is critical for the purpose of tissue repair and regeneration.

[1]Department of Biomedical and Chemical Engineering, Syracuse University, Syracuse, New York, USA.
[2]BioInspired Syracuse Institute for Material and Living Systems, Syracuse University, Syracuse, New York, USA.
[3]Department of Mechanical Engineering, University of California, Berkeley, California, USA.
*These two authors contributed equally to this article.

Opposite page: MSCs generated micropores in cell bodies on octet truss.

Image credit: System Tissue Engineering & Morphogenesis (STEM) Lab directed by Dr. Zhen Ma and Laser Thermal Lab directed by Dr. Costas P. Grigoropoulos.

Biomechanical studies are interlaced with the development of *in vitro* models using architected scaffolds.[8–10] With the emergence of multiphoton lithography (MPL), manufacturing complex three-dimensional (3D) scaffolds enabled the design of cell niches to control and regulate cell behaviors and functions.[11] The ultrahigh printing resolution of MPL makes it possible to recapitulate the nanoscopic topography of the extracellular matrix, which is necessary to create physiologically relevant models. For example, using MPL, the architecture of 3D lattice microscaffolds was found to trigger β-catenin activity of breast cancer cells through mechanotransduction pathways, which further promoted their proliferation and invasiveness.[12]

In another study, tetrakaidecahedral nanolattices with better compliance were shown to enhance the expression of f-actin and calcium secretion of osteoblast-like cells.[13] Two-dimensional auxetic structures were also found to affect the spreading of mesenchymal stem cells and division of fibroblasts.[14,15] Although many studies demonstrated the effect of lattice architecture on cellular behaviors and phenotypes, how the tissue remodeling process would affect the scaffold architecture through biomechanical interactions has not been elucidated yet.

To quantitatively understand the relationship between tissue remodeling and tissue mechanical conditions, the biomechanical models based on finite element analysis (FEA) elucidated the stress distribution within 3D microtissues and predicted their remodeling behaviors.[23–26] The accuracy of FEA is dependent on the comprehensive understanding of mechanical properties for both living tissues and biomaterial scaffolds. For example, formation of sarcomeres has been linked with the local stress state of cardiac microtissues in an FEA model to computationally simulate maturation of stem cell-derived cardiac microtissues. Furthermore, this computational simulation was used to guide the disease modeling of arrhythmogenic cardiomyopathy by modulating the tissue geometry.[27] More recently, real-time stress distribution within mouse femurs was traced by a micro-FEA model and then utilized to adapt the mechanical loading and lower the variance across all mice. This helped to prevent overloading of individual femurs, which would create bone fractures.[28]

In this work, we developed an *in vitro* tissue model based on different designs of mechanical metamaterials to study how the metamaterial architecture would affect tissue formation. Two types of thoroughly investigated metamaterials (octet-truss and auxetic bowtie structures) were fabricated by MPL using SZ2080TM, which is an inorganic–organic hybrid photoresist used for high-resolution laser fabrication. Compared with other commonly used photoresist materials, it shows negligible shrinkage during solvent washing and supports the growth of various cell types.[29–31]

Microtissues were generated by growing mesenchymal stromal cells (MSCs) derived from human induced pluripotent stem cells (hiPSCs) on metamaterial scaffolds. MSCs are widely used for general mechanobiological studies due to their presence in many tissue types and differentiation capability in response to different mechanical environments.[16–19] However, primary MSCs obtained from human donors have limited proliferation potency and high variability in cell quality.[20] To overcome these restrictions, hiPSCs have become a promising resource for MSCs because they can be expanded to a large quantity while maintaining the differentiation potential. There are already many protocols available to robustly generate MSCs from hiPSCs using small molecules and defined media.[21,22] Consistent production of MSCs from the same hiPSC source ensures model development with high robustness, consistency, and reproducibility. We found that both overall tissue morphology and local cell behaviors were highly dependent on the microarchitecture of metamaterials. Furthermore, the mechanical force generated from microtissues induced unique deformation patterns on metamaterial scaffolds, leading to structural instability due to buckling. This *in vitro* model provides the avenue to obtain a fundamental understanding of biomechanical interactions between living microtissues and metamaterial scaffolds, which will potentially be utilized to formulate new design principles to guide generation of artificial tissues for various applications.

Materials and Methods

MPL fabrication of metamaterial scaffolds

All of the metamaterial scaffolds were fabricated by the MPL process with an organic–inorganic hybrid resin, SZ2080TM, as the basal material.[32] The experimental apparatus and fabrication conditions have been reported previously.[33] Specifically, the MPL apparatus is equipped with an near infrared laser (FemtoFiber pro, Toptica) with 780 nm wavelength, 100 fs pulse width, and 80 MHz repetition rate. The laser beam was focused using a $100\times$ microscope objective lens (Plan Apochromat $100\times$/1.40 Oil M27; Zeiss). The stage was translated such that the laser beam could polymerize inside the material and fabricate the geometry. Each structure was designed in a CAD file using SolidWorks 2019x64. Through an *STL* file, it was converted into G-code so that the stages can be translated accordingly.

hiPSC-MSC differentiation

The hiPSC line was obtained from Dr. Conklin's laboratory at the University of California, San Francisco (UCSF). The committee on Human Research at UCSF approved the hiPSC research protocol (#10-02521). hiPSCs were maintained on 6-well plates coated with growth factor-reduced Geltrex (Ca# A1413302; Life Technologies) in Essential 8 (E8) medium (Ca# A1517001; Life Technologies). The protocol to differentiate hiPSC-MSCs has been published previously.[23] Briefly, hiPSCs were treated with Essential 6 (E6) medium (A1516401; Life Technologies) supplemented with 10 ng/mL basic fibroblast growth factor (Ca# 233-FB; R&D Systems), 4 μM SB431542 (Ca# 04-0010-10; Stemgent), and 4 μM CHIR99021 (Ca# 04-2004; Stemgent) for 5 days. Next, differentiated cells were dissociated and replated in a serum-free MSC culture medium (CTS StemPro MSC SFM) (A1033201; Life Technologies) for four more passages to obtain differentiated hiPSC-MSCs.

Generation of mesenchymal microtissues

To generate mesenchymal microtissues, one mechanical metamaterial scaffold was placed into one well of a 6-well plate and sterilized with 70% ethanol for 1 h. After rinsing three times with Dulbecco's phosphate-buffered saline (PBS) (Gibco), the scaffolds were then coated with diluted Matrigel for 1 h. To seed hiPSC-MSCs onto the metamaterial scaffolds, the cells were dissociated, suspended, concentrated

with a density of 1.5×10^7 cells/mL, and seeded with a total volume of 20 μL. After cell seeding, scaffolds were incubated at 37°C for 1.5 h to promote initial cell attachment before more cell culture medium was added.

Immunostaining and confocal microscopy

Architected microtissues were fixed with 4% (vol/vol) paraformaldehyde, permeabilized with 0.2% (vol/vol) Triton X-100, and blocked with 2% (wt/vol) bovine serum albumin. Next, microtissues were incubated with phalloidin for 1 h to stain F-actin and then incubated with DAPI for 10 min to stain nuclei. Confocal microscopy (U880; Zeiss) was used to capture z-stacks of the microtissues architected by the metamaterial scaffolds, which can be observed simultaneously due to autofluorescence.

Scanning electron microscopy

The microtissues were fixed in 4% paraformaldehyde overnight with 0.1 M PBS at room temperature. After washing three times with PBS, samples were then dehydrated in a series of concentrations of ethanol (15%, 30%, 50%, 70%, 95%, and 100%) at room temperature for 15 min at each concentration, plus two more 100% ethanol dehydration steps at the end. After dehydration, samples were dried in a vacuum oven for one day. Prepared samples were placed on stubs and sputter-coated with a thin layer of gold with a thickness of 10 nm. Finally, a scanning electron microscope (JSM-IT100LA; JEOL USA, Inc.) was used to image the microtissues architected by metamaterial scaffolds.

Helium ion microscopy

After sample preparation for SEM, the samples were imaged using helium ion microscopy (HIM; Zeiss ORION NanoFab). To avoid charging effects, imaging was conducted using the electron flood gun to negate the accumulating positive charge from a scanning ion beam, permitting imaging of samples without additional sputtering and allowing extremely high-resolution imaging required to observe the nanofeatures of cell membranes.

Finite element analysis

To investigate the effect of cell attachment to the scaffold, FEA simulations were performed using the multiphysics software, ANSYS R18.1. Both bowtie and octet-truss structures were discretized by 3D, 10-node, tetrahedral solid elements. Specifically, the octet-truss structure was discretized with 173018 nodes and 84558 elements, while the bowtie structure was discretized with 32301 nodes and 16648 elements. Mechanical properties were set using the same values that have been reported in the previous work.[31] Based on SEM images, cells within the bowtie structure were distributed along the edges of beam members, while cells within the octet-truss structure occupied the sides of the lattice. For this reason, a quasi-static displacement field was applied at these specific members of both lattices for large nonlinear deformations. For the bowtie structure, distributed displacement was set at the nodes of beam members at the unit edges to apply compression, while the beam members at the top were subjected to distributed displacement that would cause them to bend inward, which was represented by HIM images. For the octet-truss structure, the side beam members were subjected to distributed displacement that would cause compression of the array. Since the structures were fixed on a glass substrate, the bottom beam members were defined as fixed supports. After calculation of nonzero components of the displacement vector at each node, the force vector was obtained by the following equation:

$$\{K_o + K_u(\mathbf{u}) + K_\sigma(\boldsymbol{\sigma})\}\mathbf{u} = \boldsymbol{f}$$

where K_o is the linear stiffness matrix, $K_u(u)$ is the initial displacement stiffness matrix, $K_\sigma(\sigma)$ is the initial stress stiffness matrix, u is the displacement vector of all nodes, and f is the force vector of all the force components at respective nodes. The force–displacement curves were obtained by the reaction force at the fixed supports, which is the summation of all force vectors.

Results and Discussion

We employed two types of unit structure designs, namely octet-truss and auxetic bowtie structures, to create metamaterial scaffolds. The octet-truss structure, furnishing ultrastiff and ultralight material properties, has been used as the building block of load-bearing biomaterials for hard tissue implants.[34,35] The bowtie structure, on the other hand, is heralded by macroscopically negative Poisson's ratios, fracture resistance, and high-energy absorption performance[36,37] (Fig. 1A). Previously reported dimensions of structural units were used in our designs (octet-truss structure: beam thickness: 1.5 μm, and base length: 50 μm; and bowtie structure: beam thickness: 8 μm, and base length: 50 μm),[31,38] which ensure that the scaffolds possess the minimum volume possible while simultaneously having the structural integrity to prevent collapse. The bowtie structures had beam members with a larger diameter to prevent collapse during the fabrication process. The 3D metamaterial scaffolds were fabricated using a Ti: sapphire femtosecond laser scanning system (power: 1 mW, and scanning speed: 10 μm/s) to achieve submicron resolution in scaffold printing (Fig. 1B).[31] An organic–inorganic hybrid resin, SZ2080TM, was used as the basal material for fabricating all scaffolds.[32]

Fabricated scaffolds were imaged using scanning electron microscopy (SEM), showing precise microstructures and great mechanical integrity (Fig. 1C). The length scale of metamaterial structural units was similar to the size of individual biological cells, which would provide a direct association between biomechanical responses of cells and the structural geometry of the metamaterial unit. hiPSC-MSCs showed a spindle-like shape and expression of standard MSC markers, including CD73, CD90, and CD105 (Supplementary Fig. S1). hiPSC-MSCs were then seeded onto Geltrex-coated metamaterial scaffolds with a density of 1.5×10^7 cells/mL. The high cell seeding density resulted in formation of thick 3D tissue on metamaterial scaffolds. We estimated around four hiPSC-MSCs surrounding each structural unit of metamaterials.

On the octet-truss metamaterial scaffolds, we observed efficient penetration of hiPSC-MSCs throughout the 3D scaffolds based on the immunostaining of actin filaments and cell nuclei (Fig. 2A). Although many structural branches were present in the octet-truss structure, cells were able to traverse the struts, invade into pores within the scaffolds, and exhibit an elongated morphology. Compared with standard SEM imaging, HIM enhances the contrast, resolution, and

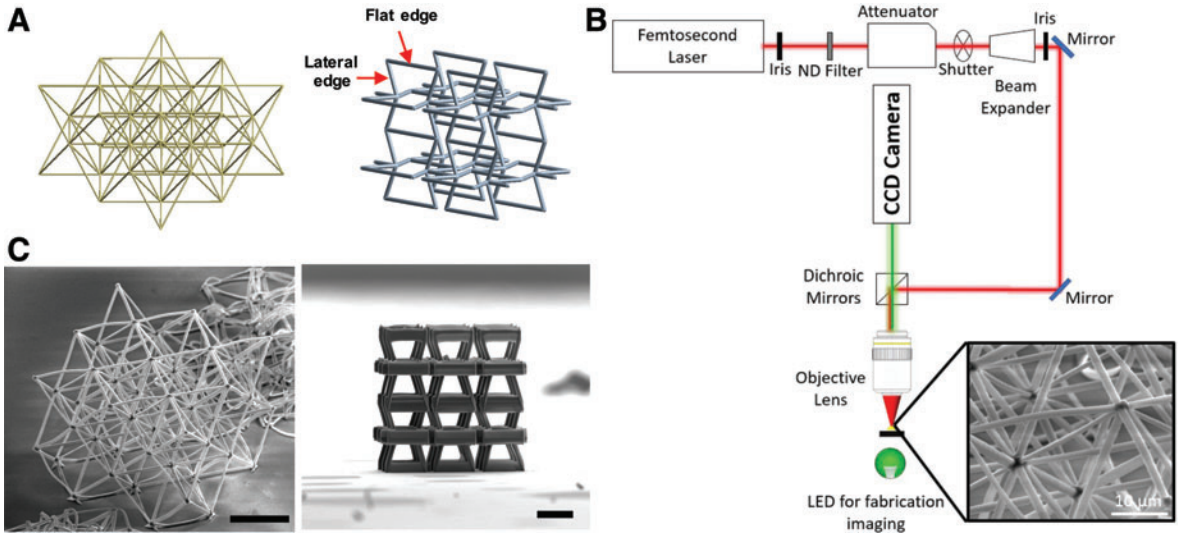

FIG. 1. Demonstration of octet-truss and auxetic metamaterials. **(A)** Diagrams of designs for two different metamaterials. The unit of octet-truss structures comprised eight tetrahedra surrounding an octahedron core. The unit of auxetic bowtie structures was made of two orthogonal reentrant honeycombs and two short arms. **(B)** Setup of the laser fabrication process using MPL. Two-photon polymerization enabled production of complex beam-based structures at high resolution. **(C)** Laser-fabricated scaffolds showed great consistency with the design files and excellent mechanical integrity. The *black* scale bar is 50 μm. MPL, multiphoton lithography. Color images are available online.

depth of field, which enable visualization of tissue–material interactions at microscopic levels.[39] To maximize attachment to metamaterials with a low material density, hiPSC-MSCs grew and elongated following the longitudinal orientation of beams, which is a common phenomenon for cells on most architected scaffolds (Supplementary Fig. S2A).[10,40,41] To further facilitate cell adhesion, thin branches of plasma membranes were extended from cell bodies to attach to adjacent beams (Supplementary Fig. S2B). In addition, micropores were present on cell bodies, which might have been created under high mechanical tension when hiPSC-MSCs spanned over different beams (Supplementary Fig. S2C).

The mechanical load generated by the microtissues led to a large deformation of the entire octet-truss metamaterial scaffold, which manifested as a decrease in its height and the inward buckling of struts at the corners (Fig. 2A). The stability of center posts maintained an isotropic stress distribution across the octet-truss structure to keep the overall integrity of the metamaterial scaffold. To define the deformation modes of metamaterials, FEA simulations were performed using the multiphysics software, ANSYS R18.1. The mechanical properties were set with the same values reported in previous work.[33] We first simulated the mechanical behaviors of the octet-truss structure under uniform mechanical

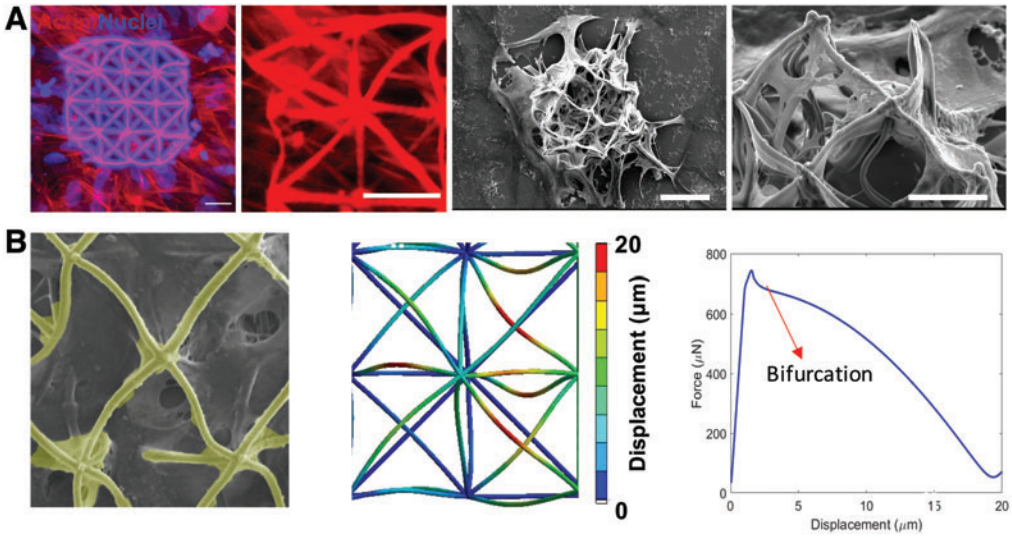

FIG. 2. Biomechanical interaction of mesenchymal microtissues on octet-truss metamaterials. **(A)** Fluorescent and SEM images showing the microtissues formed on the octet-truss metamaterial scaffolds. hiPSC-MSCs efficiently penetrated into the scaffolds and exhibited an elongated morphology. Scale bar: 20 μm. **(B)** FEA simulation results indicate that the octet-truss structure had a bifurcation buckling mode under the mechanical stress generated by the microtissues. hiPSCs, human induced pluripotent stem cells; FEA, finite element analysis; MSC, mesenchymal stromal cell; SEM, scanning electron microscopy. Color images are available online.

load. The octet-truss structure can sustain a high mechanical force without fracture with a linear relationship between force and displacement (Supplementary Fig. S4), which confirmed the ultrastiff property of this structure.

To recapitulate the deformation characteristics of octet-truss metamaterial scaffolds under the mechanical loading from microtissues, the beam members at the top part of the octet-truss structure were subjected to distributed displacement, which caused compression of the array (Fig. 2B). The bottom part attached on the coverslip, which limited the spatial moving capacity of beam members, was simulated as a fixed support. The force–displacement relationship showed that the octet-truss structure experienced a bifurcation buckling mode evidenced by the positive–negative–positive transition of the slope.[42] This distinct deformation mode indicated a unique way of mechanical loading from living biological tissues on metamaterial scaffolds.

The mesenchymal tissues growing on scaffolds formed tight connections with monolayer tissues grown on the surface of the coverslip, which applied a dominant compressive force transmitted through the main axis of beam members of the metamaterial scaffolds. Since the octet-truss structure is a stretch-dominated metastructure, the compression-induced displacement was limited by the interior hardness of materials.[43] However, the top part of the octet-truss structure had better compliance, showing that most of the beams buckled under the biological force from mesenchymal microtissues. The buckling of individual beams disrupted the integrity of the unit structure and then modulated the load-bearing mode of the octet-truss metamaterial scaffolds. Once the force was applied perpendicular to the beam axis, it was possible to deform the scaffold to a large extent with less mechanical loading.

On the auxetic bowtie metamaterial scaffolds, thicker tissue was formed with a bulky morphology and a clear tissue boundary following the contour of the scaffolds (Fig. 3A). The cells tended to aggregate around the bowtie structures with dense tissue formation instead of extending cell bodies with thin plasma membrane branches that were observed on the octet-truss metamaterial scaffolds. When imaging with HIM, we observed that cells wrapped around the beams and micropores were formed on the cell membrane (Supplementary Fig. S3A, B). The flat edges of bowtie structures were significantly deformed inward by microtissues, leading to shrinkage of their diagonal ribs and closing of pores (Fig. 3A). In addition, the vertical parts flipped 90° and met their neighbors due to the high compression force.

To simulate the deformation characteristics of bowtie metamaterial scaffolds under mechanical loading from microtissues, the distributed displacement was set at the nodes of beam members at the flat edges, while the top beams were subjected to displacement that would cause them to bend inward (Fig. 3B). The mechanical force of the microtissue caused a snap-through buckling mode on the bowtie structure demonstrated as a plateau on the force–displacement curve.[44]

Compared with the octet-truss structure, comprising multidirectional beam members that provide a homogeneous mechanical behavior, the high anisotropy degree of the bowtie structure based on its beam arrangement assured sufficient area for cell attachment without stretching the cell membrane to form thin branches. Due to disruption of structural units, the metamaterial scaffold became more compliant. However, the bowtie structure had less stress relaxation compared with the octet-truss structure since bowtie structures contained fewer buckled beams under the mechanical loading. More importantly, the negative Poisson's ratio of the bowtie structure allowed tissues to aggregate in a natural way, which brought the cells in close contact with strong intercellular connections. Hence, the entire scaffold was dramatically compressed, shown as inward buckling of individual beams at scaffold edges, flipping of vertical flat beams, and closing up of unit pores.

Results described above evidenced the fact that the mechanical load from biological tissues was prone to cause buckling of individual fibers, triggering the instability of metamaterials. However, the metamaterial scaffolds could sustain significant distortion without fracture, which possibly resulted from efficient tissue–scaffold integration as a single living composite. The active remodeling of mesenchymal microtissues made it possible to establish an equilibrium state of the composite under minimal mechanical force and energy potential. In comparison, uniform mechanical loading was passive and applied externally

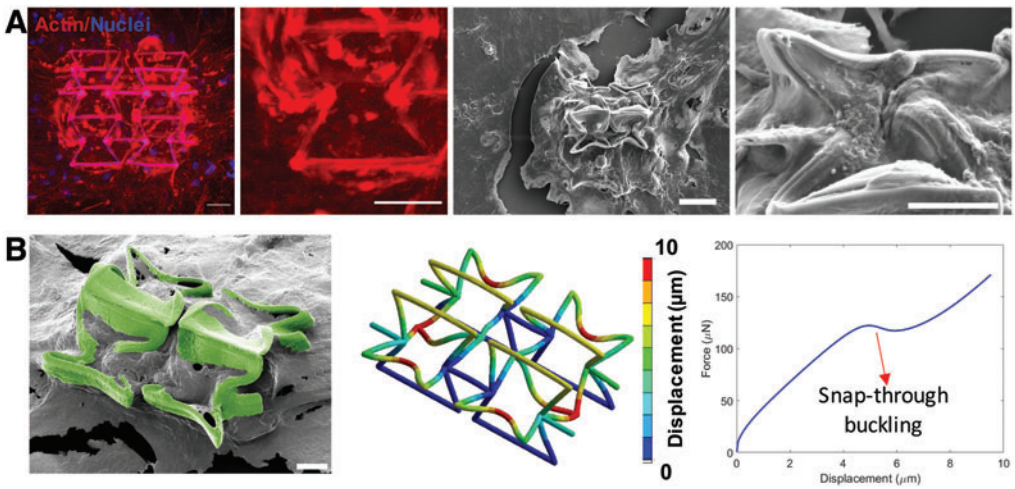

FIG. 3. Biomechanical interaction of mesenchymal microtissues on the auxetic bowtie metamaterials. **(A)** Fluorescent and SEM images showing the microtissues formed on the auxetic bowtie metamaterials. hiPSC-MSCs efficiently penetrated into the scaffolds and exhibited a bulky morphology. Scale bars: 20 μm. **(B)** FEA simulation results indicate that bowtie structures had a snap-through buckling mode under the mechanical stress generated by the microtissues. Scale bar: 20 μm. Color images are available online.

to the metamaterial scaffolds, thus it was not able to create the buckling forms that were generated internally from the living composite. The concept of living tissue–scaffold composite should be taken into consideration for future mechanistic analysis on tissue–material mechanical interaction and evolution of tissue instability.

Meanwhile, optimization of computational models is dependent on the accurate experimental measurement of spatial stiffness of the living tissue constructs. However, conventional atomic force microscopy or nanoindentation is limited for this measurement due to the highly hierarchical textures of 3D tissue constructs. Bioindenter devices are featured by their large displacement range, high-resolution force control, and capability of testing samples in a liquid condition, which are essential for measuring the mechanical properties of soft living tissues.[45–47] In future, our microtissue model can be used to establish a correlation of metamaterial geometry with soft tissue mechanics based on bioindentation measurement.

Conclusions

In summary, we have generated the first 3D human microtissue model on metamaterial scaffolds fabricated using MPL technology. hiPSC-MSCs could assemble into 3D microtissues on different metamaterial scaffolds, but tissue morphology and scaffold deformation mode were significantly different between octet-truss and bowtie structures. On the microscopic level, we observed the microtissue remodeling adapting to the complex scaffold geometry. FEA simulations revealed that mesenchymal microtissues induced different deformation modes on the metamaterial scaffolds and caused a large transformation of their geometries. Further quantification of cell surface tension, immunostaining of other cell markers, and simulation of force distribution within the metastructures would benefit a deeper understanding of how unit geometries of metamaterials affect tissue phenotypes.

Data Availability

The authors declare that all data supporting the findings of this study are available. Source data for the figures are available from the corresponding author on reasonable request.

Authors' Contributions

Z.M., C.W., Z.V., and C.P.G. conceived and designed the experiments. C.W. conducted the biological experiments and confocal microscopy. Z.V. performed the fabrication of metamaterial scaffolds. T.W. differentiated and provided the hiPSC-MSCs. S.S. performed the SEM imaging. C.W. and Z.V. analyzed and interpreted the data. C.W., Z.V., C.P.G., and Z.M. wrote the manuscript with discussions and improvements from all authors. Z.M. and C.P.G. supervised the project development and funded the study.

Acknowledgments

The authors thank Dr. Elmina Kambouraki, George Flamourakis, and Dr. Maria Farsari from FORTH for assisting in fabrication of scaffolds. The HIM experiments were conducted at the California Institute for Quantitative Biosciences (QB3).

Author Disclosure Statement

No competing financial interests exist.

Funding Information

This work was supported by the NSF (CBET-1804875, CBET-1804922, CBET-1943798, and SNM-1449305), NIH NICHD (R01HD101130), and a Syracuse University intramural CUSE Grant.

Supplementary Material

Supplementary Figure S1
Supplementary Figure S2
Supplementary Figure S3
Supplementary Figure S4

References

1. Yildizdag ME, Barchiesi E, dell'Isola F. Three-point bending test of pantographic blocks: Numerical and experimental investigation. Math Mech Solids 2020;25:1965–1978.
2. Spagnuolo M, Yildizdag ME, Andreaus U, *et al.* Are higher-gradient models also capable of predicting mechanical behavior in the case of wide-knit pantographic structures? Math Mech Solids 2021;26:18–29.
3. Kadic M, Bückmann T, Stenger N, *et al.* On the practicability of pentamode mechanical metamaterials. Appl Phys Lett 2012;100:191901.
4. Bobbert FSL, Janbaz S, Zadpoor A. Towards deployable meta-implants. J Mater Chem B 2018;6:3449–3455.
5. Ghavidelnia N, Bodaghi M, Hedayati R. Femur auxetic meta-implants with tuned micromotion distribution. Materials 2021;14:114.
6. Kolken HMA, Janbaz S, Leeflang SMA, *et al.* Rationally designed meta-implants: A combination of auxetic and conventional meta-biomaterials. Mater Horiz 2018;5: 28–35.
7. Xu S, Shen J, Zhou S, *et al.* Design of lattice structures with controlled anisotropy. Mater Design 2016;93:443–447.
8. Prasopthum A, Cooper M, Shakesheff KM, *et al.* Three-dimensional printed scaffolds with controlled micro-/nanoporous surface topography direct chondrogenic and osteogenic differentiation of mesenchymal stem cells. ACS Appl Mater Interfaces 2019;11:18896–18906.
9. Kim W, Kim M, Kim GH. 3D-printed biomimetic scaffold simulating microfibril muscle structure. Adv Funct Mater 2018;28:1800405.
10. Pennacchio FA, Caliendo F, laccarino G, *et al.* Three-dimensionally patterned scaffolds modulate the biointerface at the nanoscale. Nano Lett 2019;19:5118–5123.
11. Song J, Michas C, Chen CS, *et al.* From simple to architecturally complex hydrogel scaffolds for cell and tissue engineering applications: Opportunities presented by two-photon polymerization. Adv Healthcare Mater 2020;9:1901217.
12. Sergio S, Coluccia AML, Lemma ED, *et al.* 3D-microenvironments initiate TCF4 expression rescuing nuclear β-catenin activity in MCF-7 breast cancer cells. Acta Biomater 2020;103:153–164.
13. Maggi A, Li H, Greer JR. Three-dimensional nanoarchitected scaffolds with tunable stiffness for efficient bone tissue growth. Acta Biomater 2017;63:294–305.
14. Lantada AD, Muslija A, García-Ruíz JP. Auxetic tissue engineering scaffolds with nanometric features and resonances in the megahertz range. Smart Mater Struct 2015;24:055013.
15. Zhang W, Soman P, Meggs K, *et al.* Tuning the poisson's ratio of biomaterials for investigating cellular response. Adv Funct Mater 2013;23:3226–3232.

16. Salem HK, Thiemermann C. Mesenchymal stromal cells: Current understanding and clinical status. Stem Cells 2010;28:585–596.
17. Duarte Campos DF, Blaeser A, Korsten A, *et al.* The stiffness and structure of three-dimensional printed hydrogels direct the differentiation of mesenchymal stromal cells toward adipogenic and osteogenic lineages. Tissue Eng Part A 2015;21:740–756.
18. Hsieh WT, Liu YS, Lee Y, *et al.* Matrix dimensionality and stiffness cooperatively regulate osteogenesis of mesenchymal stromal cells. Acta Biomater 2016;32:210–222.
19. Hendrikson WJ, Rouwkema J, Van Blitterswijk CA, *et al.* Influence of PCL molecular weight on mesenchymal stromal cell differentiation. RSC Adv 2015;5:54510–54516.
20. Wang X, Lazorchak AS, Song L, *et al.* Immune modulatory mesenchymal stem cells derived from human embryonic stem cells through a trophoblast-like stage. Stem Cells 2016;34:380–391.
21. Fukuta M, Nakai Y, Kirino K, *et al.* Derivation of mesenchymal stromal cells from pluripotent stem cells through a neural crest lineage using small molecule compounds with defined media. PLoS One 2014;9:e112291.
22. Zhang L, Wang H, Liu C, *et al.* MSX2 initiates and accelerates mesenchymal stem/stromal cell specification of hPSCs by regulating TWIST1 and PRAME. Stem Cell Reports 2018;11:497–513.
23. Bose P, Eyckmans, J, Nguyen TD, *et al.* Effects of geometry on the mechanics and alignment of three-dimensional engineered microtissues. ACS Biomater Sci Eng 2019;5:3843–3855.
24. Abilez OJ, Tzatzalos E, Yang H, *et al.* Passive stretch induces structural and functional maturation of engineered heart muscle as predicted by computational modeling. Stem Cells 2018;36:265–277.
25. Walker M, Godin M, Harden JL, *et al.* Time dependent stress relaxation and recovery in mechanically strained 3D microtissues. APL Bioeng 2020;4:036107.
26. Niebur GL, Feldstein MJ, Yuen JC, *et al.* High-resolution finite element models with tissue strength asymmetry accurately predict failure of trabecular bone. J Biomech 2000;33:1575–1583.
27. Thavandiran N, Dubois N, Mikryukov A, *et al.* Design and formulation of functional pluripotent stem cell-derived cardiac microtissues. Proc Natl Acad Sci 2013;110:E4698.
28. Paul GR, Wehrle E, Tourolle DC, *et al.* Real-time finite element analysis allows homogenization of tissue scale strains and reduces variance in a mouse defect healing model. Sci Rep 2021;11:13511.
29. Pertoldi L, Zega V, Comi C, *et al.* Dynamic mechanical characterization of two-photon-polymerized SZ2080 photoresist. J Appl Phys 2020;128:175102.
30. Chatzinikolaidou M, Rekstyte S, Danilevicius P, *et al.* Adhesion and growth of human bone marrow mesenchymal stem cells on precise-geometry 3D organic–inorganic composite scaffolds for bone repair. Mater Sci Eng C 2015;48:301–309.
31. Flamourakis G, Spanos I, Vengelatos Z, *et al.* Laser-made 3D auxetic metamaterial scaffolds for tissue engineering applications. Macromol Mater Eng 2020;305:2000238.
32. Ovsianikov A, Viertl J, Chichkov B, *et al.* Ultra-low shrinkage hybrid photosensitive material for two-photon polymerization microfabrication. ACS Nano 2008;2:2257–2262.
33. Vangelatos Z, Komvopoulos K, Grigoropoulos CP. Regulating the mechanical behavior of metamaterial microlattices by tactical structure modification. J Mech Phys Solids 2020;144:104112.
34. Zheng X, Lee H, Weisgraber TH, *et al.* Ultralight, ultrastiff mechanical metamaterials. Science 2014;344:1373.
35. Arabnejad S, Johnston RB, Pura JA, *et al.* High-strength porous biomaterials for bone replacement: A strategy to assess the interplay between cell morphology, mechanical properties, bone ingrowth and manufacturing constraints. Acta Biomater 2016;30:345–356.
36. Mardling P, Alderson A, Jordan-Mahy N, *et al.* The use of auxetic materials in tissue engineering. Biomater Sci 2020;8:2074–2083.
37. Ren X, Das R, Tran P, *et al.* Auxetic metamaterials and structures: A review. Smart Mater Struct 2018;27:023001.
38. Deshpande VS, Fleck NA, Ashby MF. Effective properties of the octet-truss lattice material. J Mech Phys Solids 2001;49:1747–1769.
39. Joens MS, Huynh C, Kasuboski JM, *et al.* Helium ion microscopy (HIM) for the imaging of biological samples at sub-nanometer resolution. Sci Rep 2013;3:3514.
40. Liu Z, Wang H, Wang Y, *et al.* The influence of chitosan hydrogel on stem cell engraftment, survival and homing in the ischemic myocardial microenvironment. Biomaterials 2012;33:3093–3106.
41. Peng F, Yu X, Wei M. In vitro cell performance on hydroxyapatite particles/poly(l-lactic acid) nanofibrous scaffolds with an excellent particle along nanofiber orientation. Acta Biomater 2011;7:2585–2592.
42. Findeisen C, Hohe J, Kadic M, *et al.* Characteristics of mechanical metamaterials based on buckling elements. J Mech Phys Solids 2017;102:151–164.
43. Ruestes CJ, Farkas D, Caro A, *et al.* Hardening under compression in Au foams. Acta Mater 2016;108:1–7.
44. Rafsanjani A, Akbarzadeh A, Pasini D. Snapping mechanical metamaterials under tension. Adv Mater 2015;27:5931–5935.
45. McKee CT, Last JA, Russell P, Murphy CJ, 2011. Indentation versus tensile measurements of Young's modulus for soft biological tissues. Tissue Engineering Part B: Reviews, 17, pp.155–164.
46. Roseen MA, Fahrenholtz MM, Connell JP, *et al.* Interfacial coating method for amine-rich surfaces using poly(ethylene glycol) diacrylate applied to bioprosthetic valve tissue models. ACS Appl Bio Mater 2020;3:1321–1330.
47. Ren X, Tu V, Bischoff D, *et al.* Nanoparticulate mineralized collagen scaffolds induce in vivo bone regeneration independent of progenitor cell loading or exogenous growth factor stimulation. Biomaterials 2016;89:67–78.

Address correspondence to:
Zhen Ma
Department of Biomedical and Chemical Engineering
Syracuse University
318 Bowne Hall
Syracuse, NY 13244
USA

E-mail: zma112@syr.edu

Costas P. Grigoropoulos
Department of Mechanical Engineering
University of California, Berkeley
6129 Etcheverry Hall
Berkeley, CA 94720
USA

E-mail: cgrigoro@berkeley.edu